Journal of Materials Chemistry C

ROYAL SOCIETY OF CHEMISTRY

COMMUNICATION

View Article Online
View Journal | View Issue

Cite this: J. Mater. Chem. C, 2022, 10, 4574

Received 14th October 2021,
Accepted 1st November 2021

DOI: 10.1039/d1tc04933j

rsc.li/materials-c

Ester-functionalized thermally activated delayed fluorescence materials†

Hiroshi Tasaki,[ab] So Shikita,[ab] In Seob Park[a] and Takuma Yasuda *[ab]

A family of thermally activated delayed fluorescence (TADF) materials functionalized with carboxylate esters is presented herein. Owing to their suppressed concentration-quenching effect in neat films, these ester-functionalized TADF emitters could be applied to the fabrication of non-doped organic light-emitting diodes, demonstrating high external electroluminescence quantum efficiencies of 6.3–18.7%.

Organic thermally activated delayed fluorescence (TADF) materials have attracted significant attention because of their potential to achieve ~100% internal quantum efficiency (IQE) in organic light-emitting diodes (OLEDs). With these materials, both electrogenerated singlet (S_1) and triplet (T_1) excitons can be utilized for light emission without using precious metals.[1,2] In the electroluminescence (EL) process of TADF-OLEDs, non-radiative dark T_1 excitons can be upconverted to emissive bright S_1 excitons *via* reverse intersystem crossing (RISC) driven by ambient thermal energy. Among the vast variety of organic TADF materials ever reported, those containing carbonitrile (CN) group(s) as electron-accepting moieties occupy a prominent position because of their facile synthetic accessibility; high thermal, chemical, and electrochemical stabilities; and excellent TADF capability.[1c,3,4] As the first representative, in 2012, Adachi and coworkers reported a series of color-tuneable TADF materials based on phthalonitrile, isophthalonitrile, and terephthalonitrile tethered by multiple carbazoles.[1c] These CN-based TADF emitters afforded OLEDs with high external EL quantum efficiencies (EQEs) of up to 19.3%, because of the small singlet–triplet energy gap (ΔE_{ST}) of less than 0.1 eV. In 2016, by connecting four or five 3,6-di-*tert*-butylcarbazole (BCz) arms to a benzonitrile core, Duan and coworkers developed 2,3,5,6-tetrakis(3,6-di-*tert*-butylcarbazol-9-yl)benzonitrile and 2,3,4,5,6-pentakis(3,6-di-*tert*-butylcarbazol-9-yl)benzonitrile (**5BCzBN**) as another successful CN-based TADF family.[4] The **5BCzBN** emitter exhibited a high EQE of 21.2% and an impressive device operational lifetime of over 770 h in TADF-OLEDs. Despite the brilliant success of CN-based TADF materials, thus far, few studies have explored other isosteric electron-withdrawing groups typified by carboxylate ester (CO_2R), instead of CN.[5] Thus, exploring the applicability of ester functionalization and, thereby, expanding the chemical space for TADF emitters remains a crucial task.

Herein, we report a new family of ester-functionalized TADF emitters **1–4** (Fig. 1) that combine benzoate, isophthalate, and terephthalate esters as electron-acceptor (A) cores with four or five BCz electron-donor (D) units. Compared to the CN-based **5BCzBN**,[4] the corresponding ester-functionalized emitter (**2**) exhibited a significantly larger reorganization energy of emission (λ_S) and, thereby, a broader photoluminescence (PL) spectrum because of the larger structural relaxation of CO_2CH_3 than that of CN. Additionally, **2** exhibited a considerably high RISC rate (k_{RISC}) of over 10^6 s^{-1}, originating from an intense spin–orbit coupling (SOC) based on the ester functionalization. Non-doped OLEDs using **1–4** as neat emission layers achieved high maximum EQEs of 18.7%, 18.0%, 12.4%, and 6.3%, respectively, with relatively small efficiency roll-offs.

Compounds **1–4** were synthesized by the sequence of Fischer esterification and nucleophilic aromatic substitution (S_NAr) reactions, with commercially available fluorinated benzoic acid, isophthalic acid, and terephthalic acid employed as the starting materials. The detailed synthesis procedures and chemical characterization data are described in ESI.† Peripheral *tert*-butyl groups of BCz can serve as an insulating shell for suppressing the intermolecular electronic interactions and exciton deactivation arising from the collisional Dexter energy transfer,[6] thereby boosting the absolute PL quantum yield (Φ_{PL}) in the condensed solid states, as discussed later.

As revealed by the time-dependent density functional theory (TD-DFT) calculations (ESI†), **1–4** adopt highly distorted D–A conformations between the peripheral BCz and central

[a] *INAMORI Frontier Research Center (IFRC), Kyushu University, 744 Motooka, Nishi-ku, Fukuoka 819-0395, Japan. E-mail: yasuda@ifrc.kyushu-u.ac.jp*
[b] *Department of Applied Chemistry, Graduate School of Engineering, Kyushu University, 744 Motooka, Nishi-ku, Fukuoka 819-0395, Japan*

† Electronic supplementary information (ESI) available: Experimental procedures and characterization data. CCDC 2114087. For ESI and crystallographic data in CIF or other electronic format see DOI: 10.1039/d1tc04933j

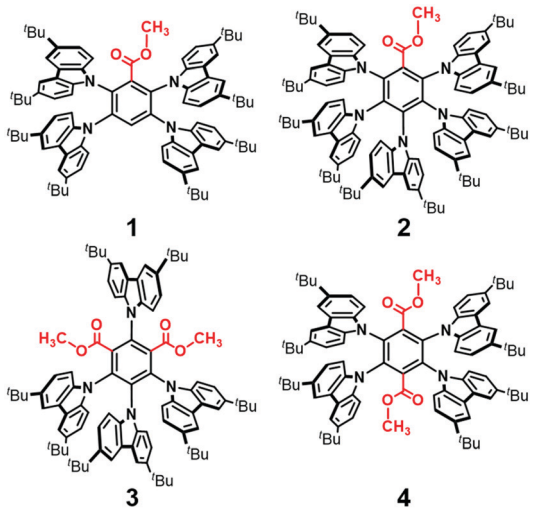

Fig. 1 Molecular structures of ester-functionalized TADF emitters **1–4**.

benzoate (or phthalate) moieties in the optimized geometries. The optimized structure of **2** exhibited large D–A dihedral angles of 60–63° in the ground (S_0) state. Accordingly, for **1–4**, the highest occupied natural transition orbitals were mainly localized on the multiple BCz units introduced, whereas the lowest unoccupied natural transition orbitals were distributed over the benzoate or phthalate core, including CO_2CH_3 substituent(s), as in the case of analogous CN-based TADF emitters.[1c,4] Such distinct spatial separations of the frontier orbitals for **1–4** resulted in ΔE_{ST} values as low as 13–25 meV in the TD-DFT calculations, suggesting the possibility of efficient ISC/RISC, followed by TADF emission.

X-Ray crystallographic analysis revealed that **2** crystallized in the triclinic space group $P\bar{1}$. In the crystal, as shown in Fig. 2, **2** was found to exist as an equimolar mixture of the enantiomeric clockwise (*C*) and counterclockwise (*CC*) propellers, similar to the case of the propeller chirality (atropisomerism) of hexaarylbenzenes.[7] To avoid steric congestion within a molecule, all five BCz propeller blades were tilted in one direction at large D–A dihedral angles of 61–69°, consistent with the foregoing calculation results. This propeller-shaped geometry would be favorable for both lowering the ΔE_{ST} and suppressing the concentration quenching.

Fig. 3a depicts the UV-vis absorption and PL spectra of **1–4** in dilute toluene solutions; the relevant photophysical data are compiled in Table 1. In addition to the intense π–π* absorption bands below 390 nm, all these molecules exhibited rather weak, broad absorptions in the range of 390–430 nm, which can be attributed to the intramolecular charge transfer (ICT) originating from their D–A electronic structures. Upon photoexcitation, **1–4** exhibited blue to orange structureless PL with emission peaks (λ_{PL}) ranging from 497 to 598 nm (Fig. 3a and b), whose Φ_{PL} values were in the order of **2** (84%) > **1** (50%) > **3** (31%) > **4** (11%) in the deoxygenated toluene solutions. As in the case of the CN-based **5BCzBN**, the ester-functionalized emitters showed a positive solvatochromism in PL[8] because of the ICT nature of the S_1 state (ESI†). Furthermore, **1–4** showed rather

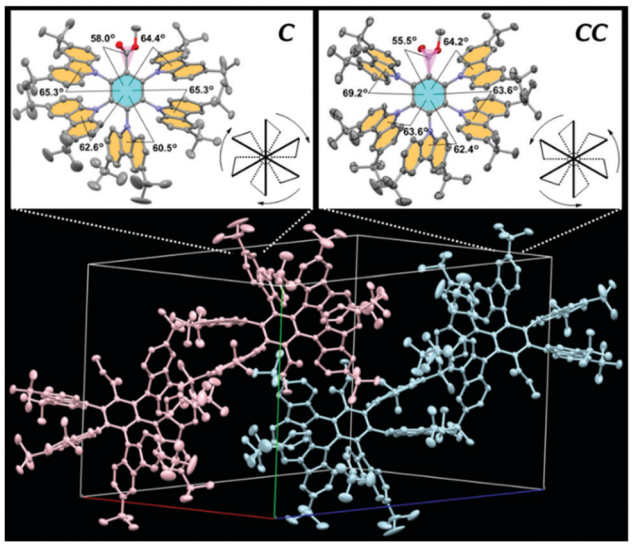

Fig. 2 Single-crystal X-ray structure of **2** (CCDC No. 2114087†) with thermal ellipsoids at 50% probability: (top) propeller-shaped enantiomeric clockwise (*C*) and counterclockwise (*CC*) isomers, and (bottom) molecular packing diagram containing equimolar *C* (pink) and *CC* (blue) isomers. The single crystals of **2** were grown from $CHCl_3/CH_3CN$ solution.

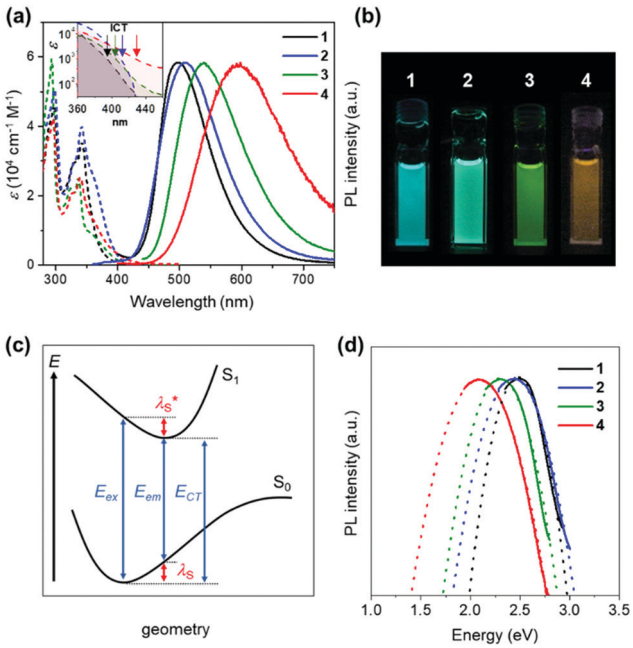

Fig. 3 (a) UV-vis absorption and PL spectra of **1–4** in toluene (1×10^{-5} M). The inset shows a magnified view of the ICT absorption bands. (b) Photograph of the PL emissions from the solutions under UV irradiation. (c) Schematic potential energy diagram of the S_0 and S_1 states; E_{ex}, E_{em}, and E_{CT} denote the energies of excitation, emission, and charge transfer, respectively. (d) PL spectra (solid lines) fitted using eqn (1) for the evaluation of λ_S.

broad PL spectra with full width at half-maxima (FWHM) as large as 99–128 nm (0.49–0.52 eV) in comparison with those of their CN-based counterparts.[1c,4] Such broadband spectral

Table 1 Photophysical data of the ester-based TADF emitters in the solution and neat films

Emitter	State[a]	λ_{PL}[b] [nm]	Φ_{PL}[c] [%]	E_{FWHM}[d] [eV]	λ_{FWHM}[d] [nm]	λ_S[e] [eV]	τ_p[f] [ns]	τ_d[f] [μs]	k_r[g] [$\times 10^6$ s^{-1}]	k_{ISC}[h] [$\times 10^8$ s^{-1}]	k_{RISC}[i] [$\times 10^6$ s^{-1}]	E_a^{ISC}[j] [meV]	E_a^{RISC}[j] [meV]
1	Sol	497	50	0.45	94	0.51	5.2	3.1	10	1.8	3.0	—	—
	Film	486	91	0.49	99	0.64	3.0	4.6	6.8	3.2	9.5	1.1	46
2	Sol	508	84	0.53	113	0.79	4.7	1.9	9.4	2.0	9.8	—	—
	Film	499	93	0.51	105	0.75	2.2	4.2	3.4	4.6	30	0.6	58
3	Sol	540	31	0.51	125	0.70	18	0.8	9.4	0.5	1.2	—	—
	Film	517	71	0.49	107	0.69	8.9	1.8	11	1.0	3.8	1.6	50
4	Sol	598	11	0.55	163	0.99	2.3	0.06	47	3.8	0.3	—	—
	Film	540	41	0.52	128	0.77	6.4	0.9	23	1.3	2.3	≈0	64
5BCzBN[k]	Sol	483	100	0.42	83	0.38	3.7	17	3.8	2.7	4.3	—	—
	Film	507	100	0.44	95	0.53	5.1	7.4	9.5	1.9	2.8	3.7	56

[a] Sol = deoxygenated toluene solution (10^{-5} M) at 300 K; film = pristine neat film at 300 K. [b] PL emission maximum. [c] Absolute PL quantum yield evaluated using an integrating sphere. [d] Full width at half-maxima of the PL spectrum given in energy and wavelength. [e] Reorganization energy along the $S_1 \rightarrow S_0$ emission estimated from the PL spectrum. [f] Emission lifetimes of the prompt fluorescence (τ_p) and delayed fluorescence (τ_d). [g] Rate constant of the fluorescence radiative decay ($S_1 \rightarrow S_0$); $k_r = \Phi_p/\tau_p$. [h] Rate constant of ISC ($S_1 \rightarrow T_1$); $k_{ISC} = (1 - \Phi_p)/\tau_p$. [i] Rate constant of RISC ($T_1 \rightarrow S_1$); $k_{RISC} = \Phi_d/(k_{ISC} \cdot \tau_p \cdot \tau_d \cdot \Phi_p)$. [j] The activation energy for ISC and RISC estimated from the Arrhenius plots of k_{ISC} and k_{RISC} (Fig. 5d). [k] See ESI.

features can be ascribed to the large structural relaxation upon the ICT ($S_0 \rightleftarrows S_1$). As schematically shown in Fig. 3c, the reorganization energies (λ_S and λ_S^*) associated with the emission and excitation processes primarily dominate the resulting spectral FWHM.[9] Thus, emitters with larger λ_S (and λ_S^*) should afford a broad ICT emission. Here, we estimated the actual λ_S values by fitting the PL spectra using the Marcus theory expression (Fig. 3d):[9,10]

$$I_{PL} \propto \frac{E}{\sqrt{4\pi\lambda_S k_B T}} \exp\left[-\frac{(E_{CT} - \lambda_S - E)^2}{4\lambda_S k_B T}\right] \quad (1)$$

where I_{PL} is the PL intensity as a function of the photon energy (E), E_{CT} is the energy difference between the S_0 and S_1 states (*cf.* Fig. 3c), k_B is the Boltzmann constant, and T is the absolute temperature. The fitted curves reasonably matched the experimental PL spectra (Fig. 3d), and large λ_S values of 0.51–0.99 eV were deduced for **1–4**. The λ_S of **2** (0.79 eV) was almost two times that of the CN-based **5BCzBN** (0.38 eV). As presented in Fig. 4, the TD-DFT calculations predicted a larger λ_S for **2** (0.73 eV) than that for **5BCzBN** (0.44 eV), which is consistent with the spectroscopic results. As evidenced by the significant change in the dihedral angle (θ) from 19° to 57° between S_1 and S_0 (Fig. 4a), the CO_2CH_3 group of **2** was found to adopt a more coplanar arrangement regarding the central benzene core in the S_1 state, whereas it adopted a highly twisted arrangement in the S_0 state. In contrast, for **5BCzBN**, negligible structural changes around the benzonitrile core were observed upon the $S_1 \rightarrow S_0$ transition (Fig. 4b). Therefore, such a large degree of structural deformation in the ester–benzene dihedral angle (θ) between the S_1 and S_0 structures should be the origin of the larger λ_S and broader PL spectrum of **2** in comparison with those of **5BCzBN**.

Fig. 5 shows the photophysical properties of **1–4** in the pure neat films (see also Table 1 for details). While intense and structureless ICT emissions were observed, the λ_{PL} positions

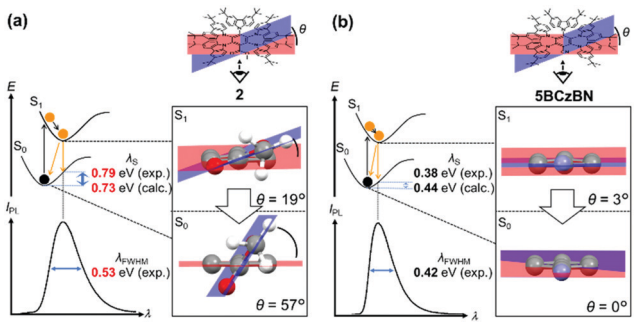

Fig. 4 Representation of the structural and spectroscopic differences between (a) **2** and (b) **5BCzBN**. Dihedral angle (θ) between the central benzene core and ester (or nitrile) group at the S_1 and S_0 geometries were simulated using TD-DFT at the PBE0/6-31G(d) level.

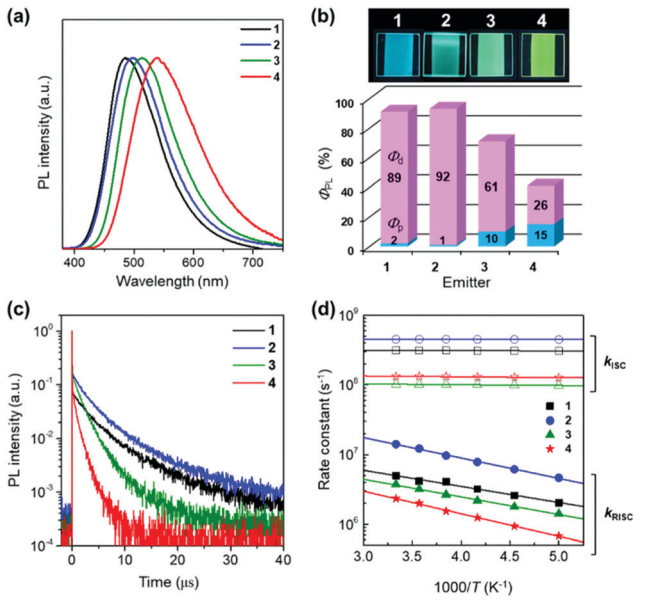

Fig. 5 (a) Steady-state PL spectra, (b) PL images and fractional quantum yields for prompt and delayed fluorescence (Φ_p and Φ_d), and (c) transient PL decay profiles of **1–4** in the neat films measured at 300 K under N_2. (d) Arrhenius plots of k_{ISC} and k_{RISC}, measured for the neat films of **1–4**, where the solid lines denote the least-squares fittings.

blue-shifted by 10–60 nm, compare to those in solutions. Notably, the neat films of **1–4** exhibited rather high Φ_{PL} values of 91%, 93%, 71%, and 41%, respectively (Fig. 5b), indicating suppressed concentration quenching even in the condensed solid states. This result is closely related to the capability of aggregation-induced emission (AIE)[11] of these propeller-shaped luminophores (ESI†). To further elucidate the TADF behaviors of **1–4**, the transient PL decay characteristics were measured for the neat films (Fig. 5c). Each of the transient PL curves clearly demonstrates two emission components at 300 K and could be fitted by a typical biexponential model. The first component with a lifetime (τ_p) of ~10 ns originates from conventional prompt fluorescence (*i.e.*, $S_1 \rightarrow S_0$), and the second, with a lifetime (τ_d) of ~10 μs, can be assigned to the TADF involving ISC and RISC (*i.e.*, $S_1 \rightarrow T_1 \rightarrow S_1 \rightarrow S_0$). We further assessed the photophysical rate constants of the fluorescence radiative decay (k_r), ISC (k_{ISC}), and RISC (k_{RISC}), as listed in Table 1. It is known that lowering the activation energy of RISC (E_a^{RISC}) can accelerate spin-flipping RISC, thereby enhancing the TADF emission.[9,12] Despite that both **2** and **5BCzBN** exhibited comparable E_a^{RISC} values of 58 and 56 meV, respectively, the k_{RISC} of **2** (3.0×10^7 s^{-1}) was found to be one order of magnitude higher than that of **5BCzBN** (2.8×10^6 s^{-1}) at 300 K. Assuming that the excited state population is described by the classical Boltzmann statistical model, k_{RISC} is given by the following equation:[9,13]

$$k_{RISC} = \frac{2\pi}{\hbar}\langle S|\hat{H}_{SOC}|T\rangle^2 \frac{1}{\sqrt{4\pi\lambda_{RISC}k_B T}} \exp\left(\frac{-E_a^{RISC}}{k_B T}\right) \quad (2)$$

where $\langle S|\hat{H}_{SOC}|T\rangle$ is the SOC matrix element between the associated T and S states, and λ_{RISC} is the reorganization energy for the RISC. As shown in Fig. 5d, eqn (2) reproduced the experimental temperature dependence of k_{RISC} for **2** with the $\langle S|\hat{H}_{SOC}|T\rangle$ value of 1.29 cm^{-1}, which was more than three times larger than that of **5BCzBN** ($\langle S|\hat{H}_{SOC}|T\rangle$ = 0.38 cm^{-1}). Therefore, the relatively fast RISC of **2** is primarily attributed to its larger $\langle S|\hat{H}_{SOC}|T\rangle$, although **2** contains no heavy metals. We anticipate that the present ester functionalization would be a simple and effective approach for enhancing SOC, thereby accelerating the spin-flipping RISC and shortening the emission lifetime.

Finally, to evaluate the EL performance of **1–4**, we fabricated non-doped TADF-OLEDs with the structure of indium-tin-oxide (ITO, 100 nm)/HAT-CN (10 nm)/TAPC (40 nm)/CCP (10 nm)/**1–4** (20 nm)/PPF (10 nm)/B3PyPB (50 nm)/Liq (1 nm)/Al (100 nm). In this device architecture, HAT-CN (2,3,6,7,10,11-hexacyano-1,4,5,8,9,12-hexaazatriphenylene) and TAPC (1,1-bis[4-[*N*,*N*-di(*p*-tolyl)amino]phenyl]cyclohexane) served as the hole-injection layer and hole-transport layer (HTL), respectively, while B3PyPB (1,3-bis[3,5-di(pyridin-3-yl)phenyl]benzene) and Liq (8-hydroxyquinolinato lithium) were adopted as the electron-transport layer (ETL) and electron-injection material, respectively. In addition, the thin layers of CCP (9-phenyl-3,9′-bicarbazole) and 2,8-bis(diphenylphosphinyl)dibenzo[*b*,*d*]furan (PPF) with high T_1 energies were inserted at the HTL/EML and EML/ETL interfaces to confine the excitons within the neat EML. Fig. 6a–c shows the EL spectra, current density–voltage–luminance (*J*–*V*–*L*) characteristics, and EQE *versus* *L* plots of devices A–D using **1–4**, and the key EL parameters are summarized in Table 2. Devices A–D were turned on at 3.6–4.0 V, and they emitted sky-blue to yellow EL with emission peaks (λ_{EL}) in the range of 494–544 nm. Among the four devices, devices A and B using **1** and **2** exhibited superior EL performance with a maximum EQE (EQE_{max}) values of 18.7% and 18.0%, respectively. Consequently, the EQE_{max} values were in the order of

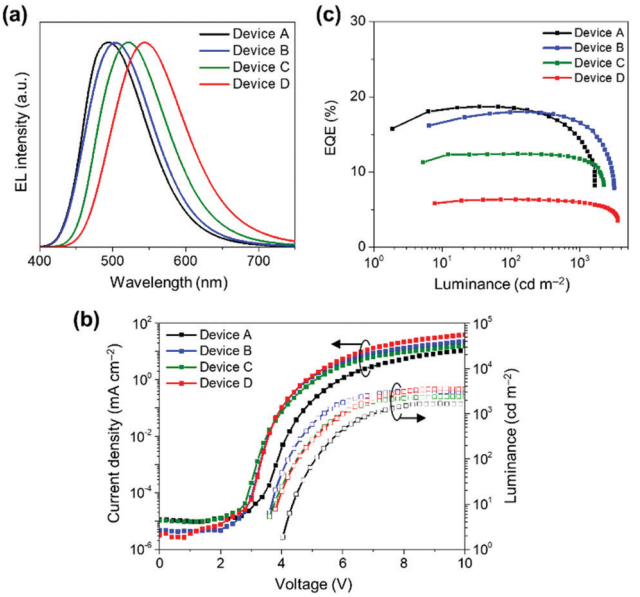

Fig. 6 (a) EL spectra, (b) current density–voltage–luminance (*J*–*V*–*L*) characteristics, and (c) EQE *vs.* *L* plots of the non-doped TADF-OLEDs based on **1–4** (Devices A–D).

Table 2 EL performance of the TADF-OLEDs based on **1–4** and **5BCzBN** (reference)

Device	Emitter	λ_{EL}[a] [nm]	E_{FWHM}[b] [eV]	λ_{FWHM}[b] [nm]	V_{on}[c] [V]	EQE_{max}[d] [%]	$EQE_{100/1000}$[e] [%]	CE[f] [cd A^{-1}]	PE[g] [lm W^{-1}]	CIE[h] (*x*, *y*)
A	**1**	494	0.49	100	4.0	18.7	18.5/13.9	46.8	37.5	(0.22, 0.40)
B	**2**	502	0.50	105	3.6	18.0	18.0/16.5	46.9	37.5	(0.24, 0.43)
C	**3**	523	0.48	108	3.6	12.4	12.4/11.6	37.0	30.6	(0.30, 0.52)
D	**4**	544	0.48	116	3.8	6.3	6.3/6.0	19.1	14.7	(0.38, 0.53)
E[i]	**5BCzBN**	512	0.45	97	3.0	15.0	15.0/14.2	43.9	41.0	(0.26, 0.49)

[a] EL emission maximum. [b] Full width at half-maxima of the EL spectrum given in energy and wavelength. [c] Turn-on voltage at a luminance of over 1 cd m^{-2}. [d] Maximum EQE. [e] EQE at a luminance of 100 and 1000 cd m^{-2}. [f] Maximum current efficiency. [g] Maximum power efficiency. [h] Commission Internationale de l'Éclairage (CIE) chromaticity coordinates. [i] See ESI.

device A (18.7%) ≈ B (18.0%) > C (12.4%) > D (6.3%) (Fig. 6c). The reason for the relatively low EQE_{max} values of devices C and D is the substantially lower Φ_{PL} values of **3** and **4** in the neat films.

In summary, a new family of TADF emitters featuring carboxylate esters was designed and synthesized. Their TADF properties were investigated through steady-state and time-resolved photophysical measurements, together with quantum chemical calculations. Compared to the well-studied CN-based analogs, the ester-functionalized TADF emitters tended to exhibit larger λ_S and k_{RISC} values. The increase in λ_S can be ascribed to the structural relaxation of the ester groups upon electronic transitions, resulting in broadband emission spectra. These ester-functionalized TADF materials exhibited rather high Φ_{PL} values even in their neat films, owing to the suppression of aggregation-caused quenching. Consequently, non-doped OLEDs based on the neat emission layers achieved high EQE_{max} values of up to 18.7%.

Conflicts of interest

There are no conflicts to declare.

Acknowledgements

This work was supported in part by Grants-in-Aid for JSPS KAKENHI (Grant No. JP21H04694), the Murata Science Foundation, and the Mitsubishi Foundation. The authors are grateful for Kyocera Corp. for generous support and helpful discussion, and for the support provided by the cooperative Research Program of the ''Network Joint Research Center for Materials and Devices'' and computer facilities at the Research Institute for Information Technology, Kyushu University.

References

1 For the earliest TADF-OLEDs, see: (*a*) A. Endo, K. Sato, K. Yoshimura, T. Kai, A. Kawada, H. Miyazaki and C. Adachi, *Appl. Phys. Lett.*, 2011, **98**, 083302; (*b*) S. Y. Lee, T. Yasuda, H. Nomura and C. Adachi, *Appl. Phys. Lett.*, 2012, **101**, 093306; (*c*) H. Uoyama, K. Goushi, K. Shizu, H. Nomura and C. Adachi, *Nature*, 2012, **492**, 234.

2 For reviews on TADF, see: (*a*) Y. Tao, K. Yuan, T. Chen, P. Xu, H. Li, R. Chen, C. Zheng, L. Zhang and W. Huang, *Adv. Mater.*, 2014, **26**, 7931; (*b*) M. Y. Wong and E. Zysman-Colman, *Adv. Mater.*, 2017, **29**, 1605444; (*c*) Y. Liu, C. Li, Z. Ren, S. Yan and M. R. Bryce, *Nat. Rev. Mater.*, 2018, **3**, 18020; (*d*) X. Cai and S.-J. Su, *Adv. Funct. Mater.*, 2018, **28**, 1802558; (*e*) X. Liang, Z.-L. Tu and Y.-X. Zheng, *Chem. – Eur. J.*, 2019, **25**, 5623; (*f*) M. Godumala, S. Choi, M. J. Cho and D. H. Choi, *J. Mater. Chem. C*, 2019, **7**, 2172; (*g*) H. Nakanotani, Y. Tsuchiya and C. Adachi, *Chem. Lett.*, 2021, **50**, 938.

3 For reviews on CN-based TADF, see: (*a*) X. Cao, D. Zhang, S. Zhang, Y. Tao and W. Huang, *J. Mater. Chem. C*, 2017, **5**, 7699; (*b*) Y. Im, M. Kim, Y. J. Cho, J.-A. Seo, K. S. Yook and J. Y. Lee, *Chem. Mater.*, 2017, **29**, 1946; (*c*) Z. Yang, Z. Mao, Z. Xie, Y. Zhang, S. Liu, J. Zhao, J. Xu, Z. Chi and M. P. Aldred, *Chem. Soc. Rev.*, 2017, **46**, 915; (*d*) J.-M. Teng, Y.-F. Wang and C.-F. Chen, *J. Mater. Chem. C*, 2020, **8**, 11340.

4 D. Zhang, M. Cai, Y. Zhang, D. Zhanga and L. Duan, *Mater. Horiz.*, 2016, **3**, 145.

5 G. Kreiza, D. Banevičius, J. Jovaišaitė, K. Maleckaitė, D. Gudeika, D. Volyniuk, J. V. Gražulevičius, S. Juršėnas and K. Kazlauskas, *J. Mater. Chem. C*, 2019, **7**, 11522.

6 (*a*) J. Lee, N. Aizawa, M. Numata, C. Adachi and T. Yasuda, *Adv. Mater.*, 2017, **29**, 1604856; (*b*) N. Aizawa, S. Shikita and T. Yasuda, *Chem. Mater.*, 2017, **29**, 7014.

7 (*a*) J. W. Rakshys. Jr., S. V. Mckinley and H. H. Freedman, *J. Am. Chem. Soc.*, 1970, **92**, 3518; (*b*) T. Kosaka, Y. Inoue and T. Mori, *J. Phys. Chem. Lett.*, 2016, **7**, 783; (*c*) C. Wang, Z.-B. Sun, Q.-W. Xu and C.-H. Zhao, *Chem. – Eur. J.*, 2016, **22**, 16750; (*d*) M. Toyoda, Y. Imai and T. Mori, *J. Phys. Chem. Lett.*, 2017, **8**, 42; (*e*) T. Kosaka, S. Iwai, Y. Inoue, T. Moriuch and T. Mori, *J. Phys. Chem. A*, 2018, **122**, 7455.

8 J. Lee, I. S. Park and T. Yasuda, *Bull. Chem. Soc. Jpn.*, 2017, **90**, 231.

9 I. S. Park, K. Matsuo, N. Aizawa and T. Yasuda, *Adv. Funct. Mater.*, 2018, **28**, 1802031.

10 (*a*) R. A. Marcus, *J. Phys. Chem.*, 1989, **93**, 3078; (*b*) I. R. Gould, D. Noukakis, L. Gomez-Jahn, R. H. Young, J. L. Goodman and S. Faid, *Chem. Phys.*, 1993, **176**, 439; (*c*) K. Vandewal, K. Tvingstedt, A. Gadisa, O. Inganäs and J. V. Manca, *Phys. Rev. B: Condens. Matter Mater. Phys.*, 2010, **81**, 125204.

11 (*a*) Y. Hong, J. W. Y. Lam and B. Z. Tang, *Chem. Commun.*, 2009, 4332; (*b*) Y. Hong, J. W. Y. Lam and B. Z. Tang, *Chem. Soc. Rev.*, 2011, **40**, 5361; (*c*) J. Mei, Y. Hong, J. W. Y. Lam, A. Qin, Y. Tang and B. Z. Tang, *Adv. Mater.*, 2014, **26**, 5429.

12 (*a*) P. K. Samanta, D. Kim, V. Coropceanu and J.-L. Brédas, *J. Am. Chem. Soc.*, 2017, **139**, 4042; (*b*) H. Noda, X. K. Chen, H. Nakanotani, T. Hosokai, M. Miyajima, N. Notsuka, Y. Kashima, J.-L. Brédas and C. Adachi, *Nat. Mater.*, 2019, **18**, 1084; (*c*) K. Matsuo and T. Yasuda, *Chem. Sci.*, 2019, **10**, 10687; (*d*) T. Agou, K. Matsuo, R. Kawano, I. S. Park, T. Hosoya, H. Fukumoto, T. Kubota, Y. Mizuhata, N. Tokitoh and T. Yasuda, *ACS Mater. Lett.*, 2020, **2**, 28; (*e*) H. Min, I. S. Park and T. Yasuda, *Angew. Chem., Int. Ed.*, 2021, **60**, 7643.

13 (*a*) N. Aizawa, A. Matsumoto and T. Yasuda, *Sci. Adv.*, 2021, **7**, eabe5769; (*b*) I. S. Park, H. Min, J. U. Kim and T. Yasuda, *Adv. Opt. Mater.*, 2021, **9**, 2101282.

